

# Screening of F-containing electrolyte additives and clarifying their decomposition routes for stable Li metal anodes

Received: 8 February 2024

Accepted: 21 October 2024

Published online: 29 October 2024



Jijiang Liu<sup>1,4</sup>, Wei Hao<sup>1,2,4</sup>, Mingming Fang<sup>1,4</sup>, Xin Chen<sup>1,3,4</sup>, Yonteng Dong<sup>1</sup>, Yuanmao Chen<sup>1</sup>, Zhiyong Wang<sup>1</sup>, Xinyang Yue<sup>1</sup>✉ & Zheng Liang<sup>1</sup>✉

Constructing a LiF-rich solid electrolyte interphase (SEI) is a feasible strategy for inhibiting lithium (Li) dendrites of Li metal anodes (LMAs). However, selecting appropriate F-containing additives with efficient LiF contribution is still under active research. Herein, a series of fluorinated additives with diverse F/C molar ratios are investigated, and we demonstrate that the hexa-fluoroglutaric anhydride ( $F_{6-0}$ ) holds the best capability to derive the LiF-rich SEI in regular carbonate electrolytes (RCEs). To ameliorate the decomposition kinetics of the  $F_{6-0}$ ,  $LiNO_3$  (LNO) as an adjuvant is further introduced in the system. As a result, the reduction efficiency of  $F_{6-0}$  is increased to 91% under the  $F_{6-0}$ /LNO synergistic effect, enabling the LMA with a uniform LiF-rich SEI in the RCE with merely 4 vol. %  $F_{6-0}$ /LNO (F6L) addition. The  $LiNi_{0.8}Co_{0.1}Mn_{0.1}O_2$ ||Li-20 $\mu$ m full-cell with the F6L also showcases better cycling and rate performances than the cases with other F-containing additives.

Rechargeable lithium metal batteries (LMBs) represent one of the most promising high-energy-density battery technologies for next-generation applications<sup>1,2</sup>. However, the unstable Li metal anodes with dendrite formation trigger fast capacity fading and safety hazards<sup>3</sup>, hindering the application of LMBs. Constructing a LiF-rich solid electrolyte interphase (SEI) has been universally acknowledged as crucial for achieving uniform Li plating/stripping and suppressing Li dendrite growth<sup>4–7</sup>. Owing to its high Young's modulus, high surface energy, and abundant Li-ion flux, the LiF-rich SEI effectively dissipates the local current density to tune the Li nucleation in a uniform and low-volume manner, reducing the tendency of the moss-like dendrite growth<sup>8</sup>. Efforts to create a LiF-rich SEI have primarily focused on enhancing the F content of electrolytes<sup>9–12</sup>. Using high-concentration electrolytes (HCE) and localized high-concentration electrolytes (LHCE) can in-situ form a LiF-rich SEI<sup>13–16</sup>, but its high cost greatly limits its feasibility. In this regard, the introduction of an F-containing additive (<10 vol. %) (denoted as F-additive) in regular carbonate electrolytes (RCE) seems to be a better approach.

When choosing an F-additive, the first thing that needs to be considered is that a high F/C molar ratio is more likely to enhance the formation of LiF at the Li metal interface. Besides, the F-additive should be capable of dissolving in electrolytes without any separation. Furthermore, the lowest unoccupied molecular orbital (LUMO) energy is necessary for an F-additive to achieve a complete reduction and fast film-forming during the initial few cycles<sup>17–19</sup>. However, the major bottleneck is that current F-additives are hard to meet the above three requirements at the same time. For example, fluoroethylene carbonate (FEC, **1**) is a proven film-forming additive for the SEI<sup>20</sup>, but its F/C molar ratio (0.33:1) is low (Fig. 1a). Fluorinated ether solvents, such as 1,1,2,2-tetrafluoroethyl 2,2,3,3-tetrafluoropropyl ether (HFE, **5**) and 1,1,2,2-tetrafluoroethyl 2,2,2-trifluoroethyl ether (TFTE, **6**), have high F/C molar ratio but showing electrochemically inert to Li-ion coordination and LiF decomposition, so they have so far only been developed as diluents<sup>21</sup>. Given the variations of orbital energy levels in coordinating solvents, the perfluoro-substituted anhydride featured with high F/C molar ratios could be seen as a

<sup>1</sup>Frontiers Science Center for Transformative Molecules, School of Chemistry and Chemical Engineering, Shanghai Jiao Tong University, Shanghai, China.

<sup>2</sup>Department of Electrical Engineering, Shanghai Jiao Tong University, Shanghai, China. <sup>3</sup>Department of Physics and Astronomy, University of California Los Angeles, Los Angeles, CA, USA. <sup>4</sup>These authors contributed equally: Jijiang Liu, Wei Hao, Mingming Fang, Xin Chen. ✉e-mail: [xinyangyue@sjtu.edu.cn](mailto:xinyangyue@sjtu.edu.cn);

[liangzheng06@sjtu.edu.cn](mailto:liangzheng06@sjtu.edu.cn)



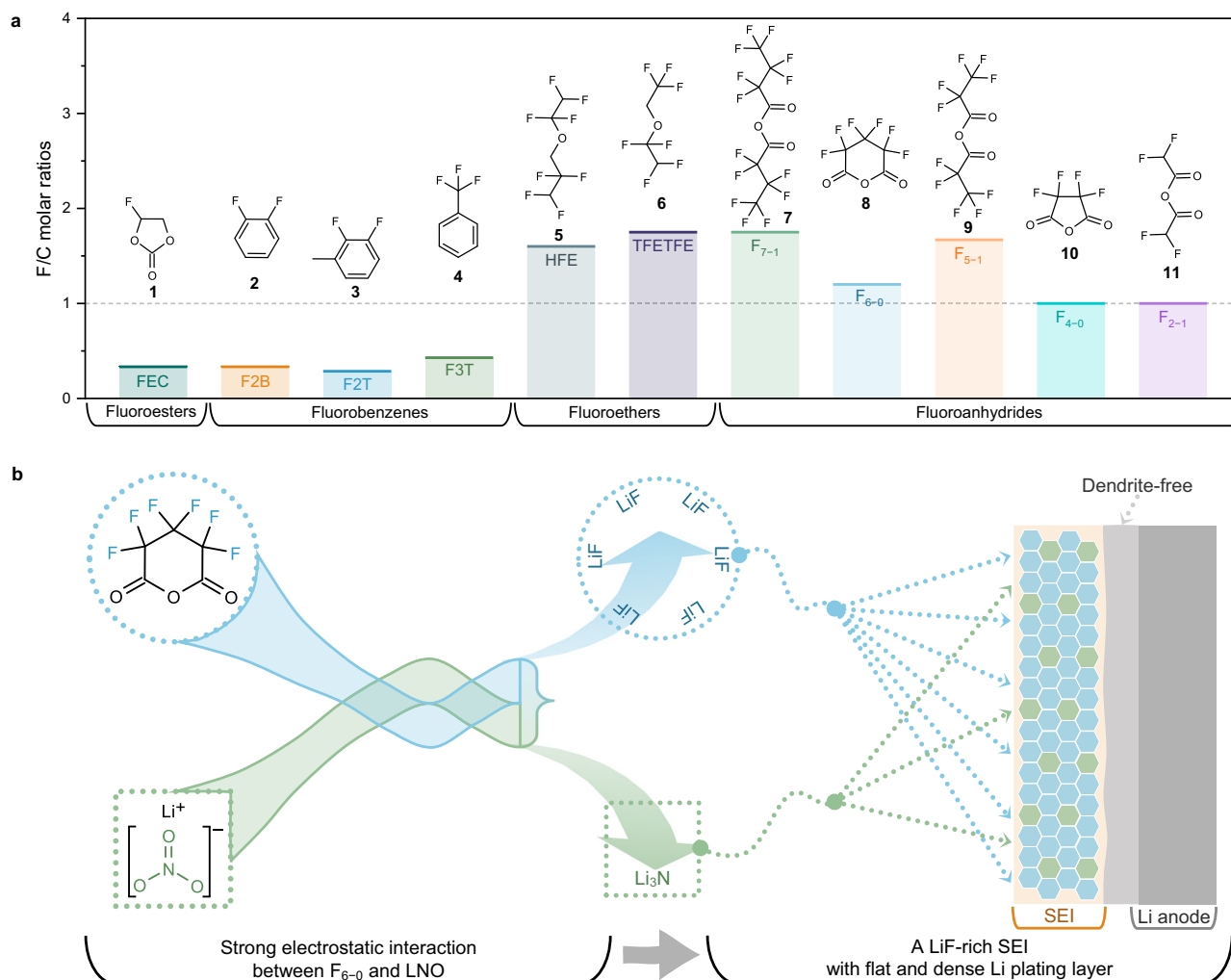


**Fig. 1 | Working mechanisms of the selected F-containing additive and its synergistic effect with LiNO<sub>3</sub>.** **a** The F/C molar ratios of the various F-containing additives. **b** Schematic diagram of achieving highly uniform and dendrite-free Li

plating by constructing the inorganic LiF-rich SEI on Li anode with F6L. Source data are provided as a Source Data file.

candidate for ideal F-additives. Lucht et al. demonstrated in early reports that the fluorinated anhydride additives are capable of participating in the SEI formation, but the LiF contents in the SEI did not improve as expected<sup>22</sup>. This phenomenon is primarily due to the high chemical stability of the fluorinated anhydride. In this sense, tuning the C–F bond of the perfluoro-substituted anhydride to be more easily broken and reduced is a crux for developing an F-additive, yet relevant research has rarely been reported.

In this work, we propose a hexafluoroglutaric anhydride (F<sub>6-0</sub>, **8**)/LiNO<sub>3</sub> (LNO) (denoted as F6L) as an F-additive to endow Li metal anodes with a LiF-rich SEI in RCEs (Fig. 1b). The first-principles calculations and the in-situ Fourier transform infrared reflection (FTIR) spectroscopy are carried out to decipher the relative energy evolution during the decomposition of F<sub>6-0</sub> to eventual LiF. The results demonstrate that the mutual interaction between the F<sub>6-0</sub> and LNO prompts the transformation of the C–F bonds in F<sub>6-0</sub> from covalent to more readily breakable ionic bonds, elevating the F<sub>6-0</sub> reduction ratio from the original 3.1% up to 91%. Therefore, a 4 vol. % F6L addition allows a significant increase of LiF contents in SEI, enabling both the Li symmetric cell and high-loading LiNi<sub>0.8</sub>Co<sub>0.1</sub>Mn<sub>0.1</sub>O<sub>2</sub>||Li-20 μm (NCM811||Li) full-cell with improved rate capability and long-term cycling performance. Moreover, the self-made 1.0-Ah LiFePO<sub>4</sub>||Li-20 μm (LFP||Li) pouch cells and the cost of the F6L electrolyte are assessed, verifying the high feasibility of F6L for practical LMAs.

## Results

### Optimizing the compositions of F6L

The molecular structure of F<sub>6-0</sub> is depicted in Fig. 1a, which shows that the F/C molar ratio for F<sub>6-0</sub> is 1.2, much higher than that of the FEC (0.33). The F<sub>6-0</sub> also exhibited good solubility in the RCE composed of 1 M LiPF<sub>6</sub> in ethylene carbonate (EC)/dimethyl carbonate (DMC) (1:1, v/v) (Fig. 2a), while the related linear anhydrides, such as heptafluorobutyric anhydride (F<sub>7-1</sub>, **7**), were difficult to dissolve in RCE. Generally, the interaction force of circular molecules is usually much stronger than that of linear ones, so the F<sub>6-0</sub> additive amount in RCE could reach over 20 vol. % at room temperature. More importantly, although the F/C molar ratio for F<sub>6-0</sub> is slightly lower than that for F<sub>7-1</sub>, the C–F bond energy of the former is significantly lower than that of the latter and other fluorinated anhydrides, implying that F<sub>6-0</sub> is relatively easily reduced by the electrochemical process (Supplementary Fig. 1). Another advantage of F<sub>6-0</sub> is that the double C=O bonds in anhydride promote the dissociation of LNO in RCE by stabilizing the dissolved ions (Fig. 2b). One of the carbonyl groups of F<sub>6-0</sub> interacts with Li<sup>+</sup> and forms part of the solvation shell, while the other carbonyl group remains free due to factors such as steric hindrance and solvation energy optimization<sup>23</sup>, thus hindering the recombination of Li<sup>+</sup> and NO<sub>3</sub><sup>−</sup> through electrostatic repulsion. This structure raises the activation energy of the deposition process (ΔE<sub>3, Deposition</sub>), significantly enhancing the solubility of LNO in RCE

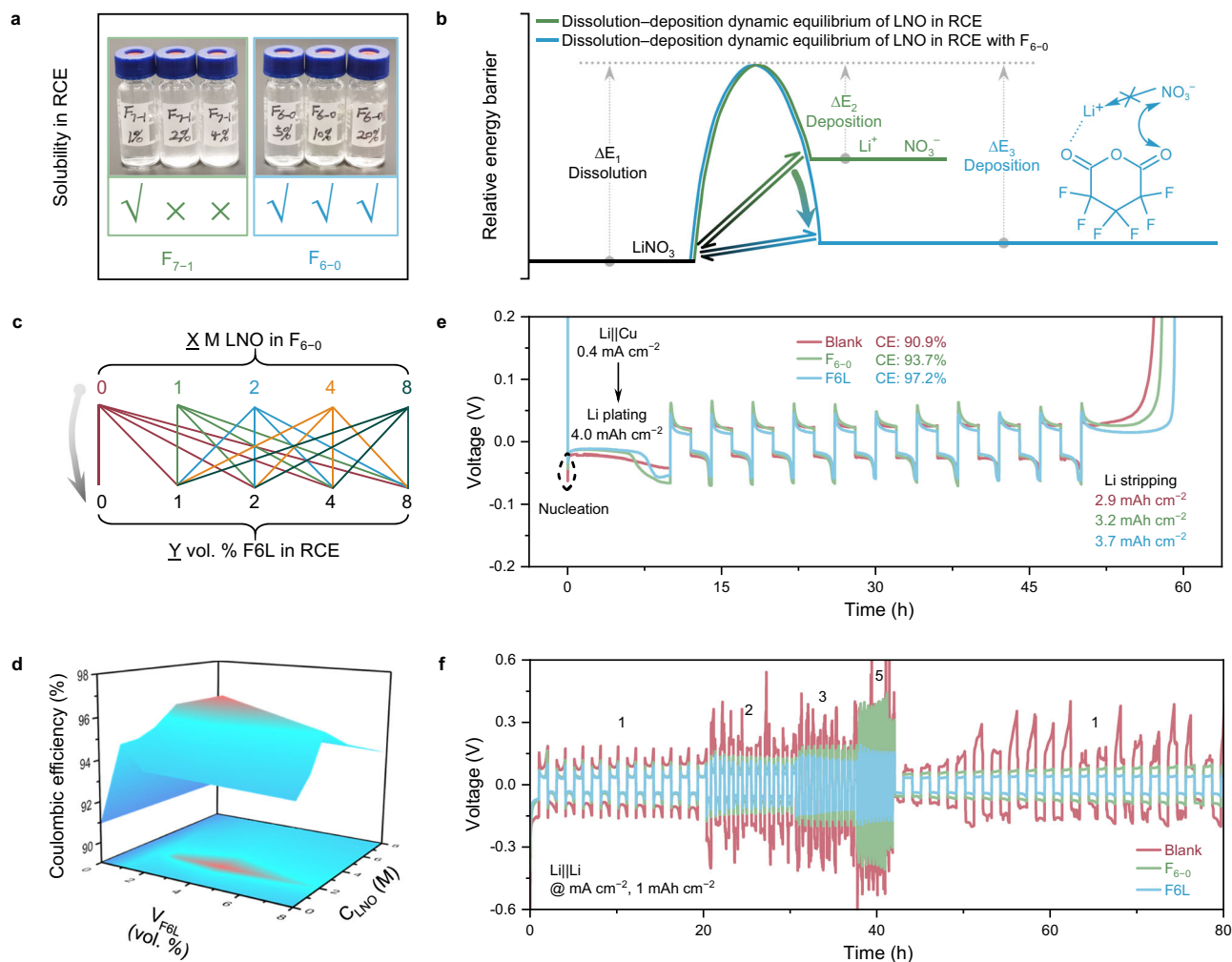


**Fig. 2 | Optimizing the composition of F6L.** **a** The solubility of  $F_{6-0}$  and  $F_{7-1}$  in the RCE. **b** The illustration of the dissolution–deposition dynamic equilibrium of LNO in the RCE<sup>23</sup> without and with  $F_{6-0}$ . **c** The schematic of regulating the components of F6L. **d** Contour plots of CEs recorded from the half-cells using the RCE with F6L.

having various ratios of  $F_{6-0}$  and LNO at  $0.4 \text{ mA cm}^{-2}$  with  $0.8 \text{ mAh cm}^{-2}$ . **e** Voltage profiles of half-cells using Blank,  $F_{6-0}$ , and optimized F6L. **f** The rate performance of Li symmetric cells using Blank,  $F_{6-0}$ , and optimized F6L. Source data are provided as a Source Data file.

with  $F_{6-0}$ . Therefore, a homogeneous  $F_{6-0}$ /LNO (F6L) composite solution with a synergistic effect between  $F_{6-0}$  and LNO was established as a prototyped F6L for the following study.

Twenty-one different ratios of  $F_{6-0}$  and LNO were sequentially designed according to concentration gradients to screen and obtain the optimal formulation for F6L. Two variables were controlled in the preparation of the F6L, which are the concentration of LNO in  $F_{6-0}$  ( $C_{\text{LNO}}$ ) and the amount of addition of F6L in RCE ( $V_{\text{F6L}}$ ). The  $C_{\text{LNO}}$  (M) and  $V_{\text{F6L}}$  (vol. %) for target samples are 1, 2, 4, and 8 (Fig. 2c, Supplementary Fig. 2, and Supplementary Table 1), respectively. All the electrolytes were evaluated via the Li plating/stripping reversibility of the Li||Cu half-cells, in which the Coulombic efficiency (CE) was calculated based on Aurbach's method<sup>24,25</sup>. The results of the CE are summarized in Fig. 2d. It can be seen in contour plots that the highest CE (97.2%) was attained when 4 vol. % F6L containing 2 M LNO in  $F_{6-0}$  (2LNO +  $F_{6-0}$ ) was added into RCE, which is 6.3% higher than the blank RCE (Blank), indicating the effectiveness of this optimized F6L-derived SEI in suppressing Li dendrite growth (Supplementary Fig. 3). By contrast, the CE of the cell with 4 vol. % single  $F_{6-0}$  or LNO additive was only 93.7% or 91.3%, respectively. The Li nucleation polarization for optimized F6L,  $F_{6-0}$ , RCE + LNO, and Blank cells was measured at 32.5, 43.6, 50.7, and 62.5 mV (Fig. 2e and Supplementary Fig. 4), respectively, which implies that the SEI formed in optimized F6L could

facilitate the Li nucleation process. Moreover, the resulting SEI also featured high Li-ion transport kinetics, as proved by the rate performance of the Li symmetric cells (Fig. 2f, Supplementary Figs. 5 and 6). Based on the above analysis, a 4 vol. % optimized F6L (2LNO +  $F_{6-0}$ ) was selected as the studied F-additive in RCE. The counterparts include the RCE with  $F_{6-0}$  and RCE with LNO, denoted as F6 and RCE + LNO, respectively.

### Analysis of the F6L-derived SEI

To determine the chemical structure of the SEI, the X-ray photoelectron spectroscopy (XPS) depth profiling was conducted on the Li metal surface after initial cycles. The Ar-ion etching rate is *ca.*  $0.04 \text{ nm s}^{-1}$ . The results of the XPS spectra on the chemical states of SEI and the corresponding binding energy are listed in Supplementary Table 2. For the Blank (Fig. 3a), the chemical species states of R–O–CO<sub>2</sub>– (at  $-289.9 \text{ eV}$ ) and C=O (at  $-288.4 \text{ eV}$ ), which was generated from the decomposition of the carbonate solvents (EC and DMC), indicating the solvent-derived organic components of the SEI. After adding F6, a new peak at  $291.1 \text{ eV}$  emerged, which can be assigned to the F–C–F of the  $F_{6-0}$  (Fig. 3b). When the detecting depth reached  $\sim 5 \text{ nm}$ , the F–C–F peak disappeared and a C–F peak at  $292.0 \text{ eV}$  emerged, corresponding to the F–C–F bond cleavage. As to the F6L sample, its C 1s XPS spectra reveal that the  $F_{6-0}$  signal is mainly reflected by the C–F peak rather

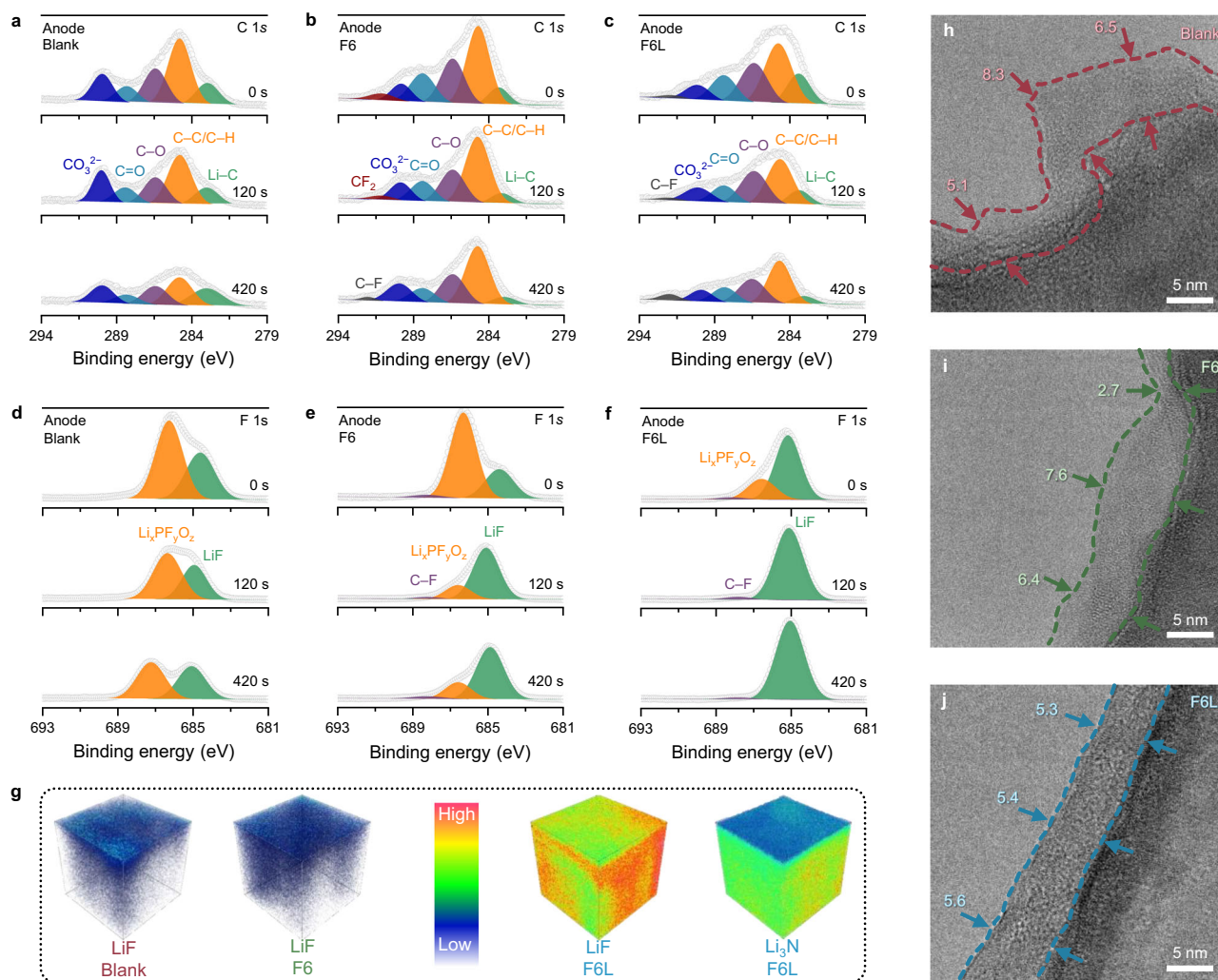


**Fig. 3 | Characterization of SEI on the Li metal surface.** In-depth C 1s XPS spectra of Li metal anodes after 20 cycles in **a** Blank, **b** F6, and **c** F6L. In-depth F 1s XPS spectra of Li metal anodes after 20 cycles in **d** Blank, **e** F6, and **f** F6L. **g** TOF-SIMS

depth profiles of SEIs formed in Blank, F6, and F6L. Cryo-TEM images of SEIs formed in **h** Blank, **i** F6, and **j** F6L. Source data are provided as a Source Data file.

than the F–C–F peak at all thicknesses (Fig. 3c), indicating the higher decomposition rate of the F6L as compared to the F6.

In the F 1s XPS spectra of Blank (Fig. 3d), the LiF and  $\text{Li}_x\text{PF}_y\text{O}_z$  originated from the decomposition of  $\text{LiPF}_6$  in RCE and served as the inorganic components of the SEI<sup>26</sup>. Adding F6 could somewhat increase the LiF content in the SEI, but the reduction of F6 is still low, as confirmed by the stronger  $\text{Li}_x\text{PF}_y\text{O}_z$  peak (Fig. 3e). By contrast, due to the improved decomposition of the F6L, the LiF peak became dominant in F 1s XPS spectra of the F6L sample at different thicknesses (Fig. 3f). The reduced intensity of the  $\text{Li}_x\text{PF}_y\text{O}_z$  peak in F6L XPS spectra means that the LiF layer formed by preferential decomposition of F6L hinders the reduction of  $\text{LiPF}_6$ , which is in line with the observation in the P 2p and O 1s XPS spectra (Supplementary Figs. 7 and 8). In addition to LiF, LNO-derived  $\text{Li}_3\text{N}$  was also uniformly distributed inside the SEI formed by F6L (Supplementary Figs. 9 and 10), emphasizing not only the strong electrostatic interaction of  $\text{F}_{6-0}$ /LNO but also the role of  $\text{F}_{6-0}$  in inducing the decomposition of  $\text{NO}_3^-$  anion.

TOF-SIMS was utilized to investigate the spatial stereoscopic distribution of the inorganic component in SEI (Fig. 3g). The SEI formed in Blank shows an uneven LiF distribution due to the weak inorganic-film-forming property of the  $\text{LiPF}_6$ <sup>27</sup>. In F6, the LiF distribution inside the SEI was uneven due to the sluggish kinetics of the  $\text{F}_{6-0}$  decomposition. In sharp contrast, a three-dimensional uniformly

distributed LiF layer was observed in the F6L-derived SEI. Besides, the  $\text{Li}_3\text{N}$  distribution in this SEI was also uniform and highly overlapped with the LiF distribution. This result is in accordance with the XPS analysis. The SEIs were further investigated using cryogenic transmission electron microscopy (cryo-TEM) techniques. Figure 3h, i, Supplementary Fig. 11a, b demonstrate that the SEIs were gradually thickened and appeared rough morphology in both Blank (from ~6.5 to ~13.6 nm) and F6 (from ~6.4 to ~13.7 nm) after 20 and 50 cycles. In contrast, the F6L-derived SEI was thinner (~5.5 nm) and uniform and could remain stable over the cycles (Fig. 3j and Supplementary Fig. 11c). In short, the decomposition kinetics of  $\text{F}_{6-0}$  to LiF could be accelerated in RCE under the assistance of LNO, resulting in a uniform and dense SEI dominated by LiF on Li metal anodes.

### Decomposition chemistry of F6L

To unveil how the  $\text{F}_{6-0}$  and F6L decompose, the first-principles calculation based on density functional theory (DFT) was conducted. The impact of LNO on  $\text{F}_{6-0}$  under static conditions was first analyzed. The structural geometries employed to compute C–F bond energies and electronic structure are displayed in Supplementary Fig. 12. As displayed in Fig. 4a, the average bond energy of C–F in  $\text{F}_{6-0}$  decreased by 12.6% when the LNO molecule approached the  $\text{F}_{6-0}$  molecule, indicating a stronger interaction of  $\text{F}_{6-0}$ /LNO. The LUMO/highest occupied

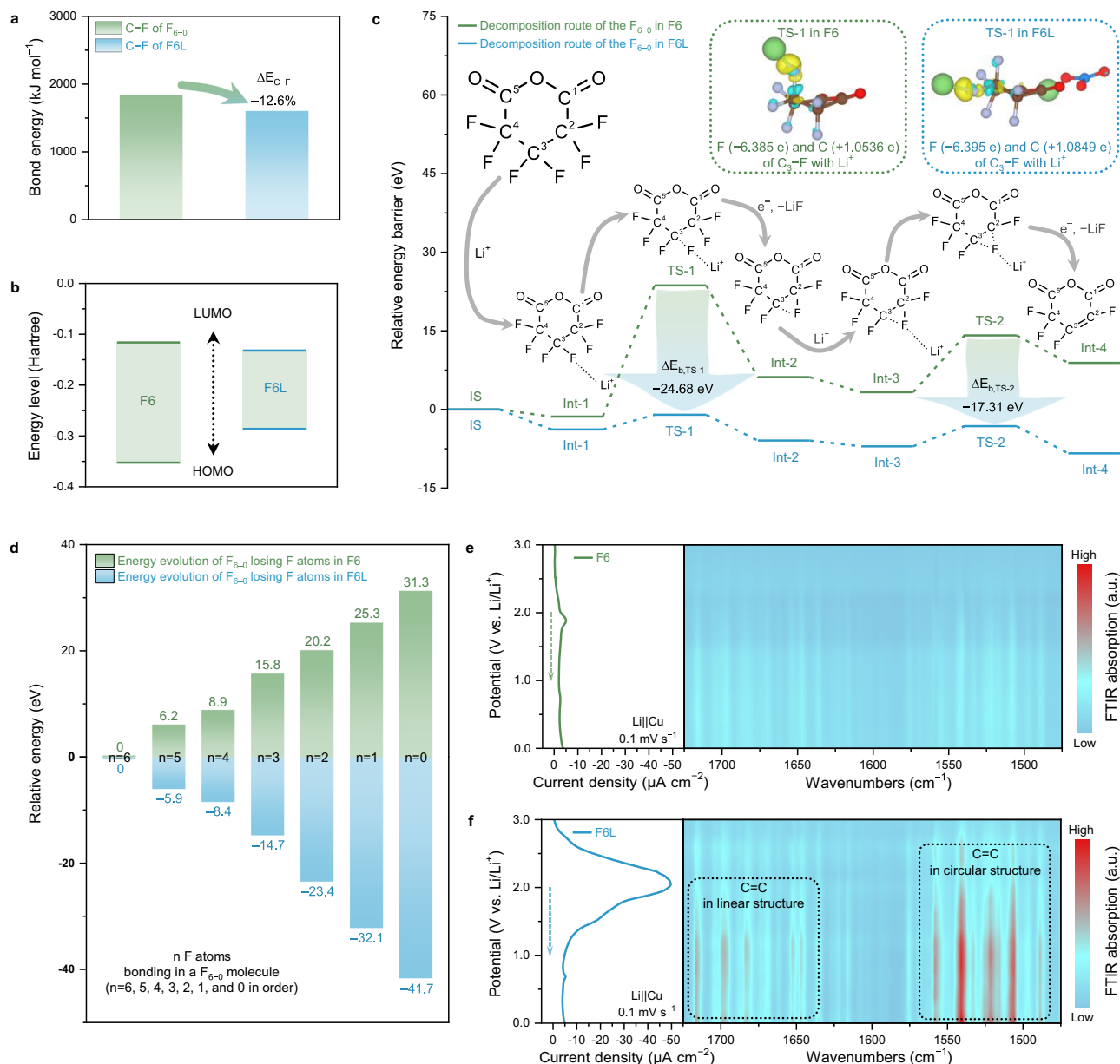


**Fig. 4 | Clarification of the decomposition routes of  $F_{6-0}$ .** **a** The average C–F bond energy in the  $F_{6-0}$  and F6L. **b** The LUMO and HOMO energy levels of F6 and F6L. **c** The energy diagram of the first two steps of  $F_{6-0}$  towards complete decomposition with their corresponding energy barriers for each reaction process. Insets show the charge density difference isosurfaces ( $\pm 0.04 \text{ e}/\text{\AA}^3$ ) and Bader charge of C and F in  $C^3\text{--F}$  for F6 and F6L, where the yellow and blue isosurfaces indicate the

charge density increase and decrease, respectively. The green, brown, blue, red, and light blue balls represent Li, C, N, O, and F atoms, respectively. **d** The energy evolution of the entire decomposition process for  $F_{6-0}$  in F6 and F6L. Electrochemical in-situ FTIR spectra of Li||Cu half-cells using **e** F6 and **f** F6L at  $0.1 \text{ mV s}^{-1}$ . Source data are provided as a Source Data file.

molecular orbit (HOMO) energy levels of the  $F_{6-0}$  were also affected by LNO. As Fig. 4b shows, because of the low LUMO energy level, the  $F_{6-0}$  in F6L featured a propensity for reducing and decomposing preferentially on Li metal surfaces than the  $F_{6-0}$  in F6.

Figure 4c presents the decomposition routes of the  $F_{6-0}$  and the relevant energy changes under dynamic conditions. The decomposition process could be divided into six steps corresponding to the formation order of LiF. The first two steps are chosen as the example for brief elucidation since they represent the most challenging energy barriers (rate-limiting steps) to overcome. The first step is the generation of the first LiF product, which involves the initial state (IS), the intermediate state (Int-1), the transition state (TS-1), and the second intermediate state (Int-2). The second step contains the process of

generating the second LiF product, which involves the third intermediate state (Int-3), the second transition state (TS-2), and the fourth intermediate state (Int-4). For Step 1, the  $C^3\text{--F}$  bond is weakened by the electrostatic attraction of Li-ions, and the electron-rich F atom is then captured to form the first LiF. The main energy barrier is generated in the process from Int-1 to TS-1 (denoted as  $\Delta E_{b, \text{TS-1}}$ ). The  $\Delta E_{b, \text{TS-1}}$  for F6 and F6L is 25.03 and 2.81 eV, respectively, indicating that the first  $C^3\text{--F}$  bond in F6L is more likely to break as opposed to what occurs in F6.

The chemical activity of  $C^3\text{--F}$  bonds in  $F_{6-0}$  is affected by the inductive effect induced by the anhydride group ( $\text{O}=\text{C}\text{--O}\text{--C}=\text{O}$ )<sup>28</sup>. The inductive effect brought by the C=O group is transferred to the C3 atom and attracts the electron-pair of the  $C^3\text{--F}$  bond towards the  $C^3$  atom, resulting in a relatively less positively-charged state than



other C atoms (Supplementary Fig. 13). Once a Li-ion appears near the F atom, the electronic density of the C–F bond will decrease (Fig. 4c). Thus, the covalent component of the C<sup>3</sup>–F bond is reduced, with the ionic component increasing, eventually resulting in the cleavage of the C<sup>3</sup>–F bond and the formation of LiF. Whereas for F6L, the presence of the NO<sub>3</sub><sup>−</sup> near the C<sup>1</sup>=O group of F<sub>6-0</sub> pushes  $\pi$  electrons toward C<sup>1</sup>, reducing the inductive effect acting on C<sup>3</sup>. Therefore, the C<sup>3</sup>–F bonding electrons tend to shift towards the F side, enhancing the electronic density of the F atom (Supplementary Fig. 14). This behavior is also supported by the Bader charge analysis, demonstrating that the F atom of C<sup>3</sup>–F with Li-ion under TS-1 in F6L is negatively charged at −6.395 e, a value more negative than that (−6.385 e) in F6. Accordingly, the C<sup>3</sup>–F bond in F6L has a higher ionic component than that in F<sub>6-0</sub> under the same conditions, lowering the  $\Delta E_{b, \text{IL-T1}}$  in the F6L system. Similarly, when Li-ion approached the F atom, the charge density difference analysis exhibited the weakening of the C<sup>3</sup>–F bond and the strengthening of the Li–F bond.

Upon Step 2, the F atom in the C<sup>2</sup>–F bond is attacked by Li-ion and captured to form the second LiF, with the resulting unsaturated C<sup>2</sup> and C<sup>3</sup> simultaneously forming a double bond. Similar to Step 1, the NO<sub>3</sub><sup>−</sup> in F6L accelerates the cleavage of the C<sup>2</sup>–F bond. Thereby, the  $\Delta E_{b, \text{I3-T2}}$  for F6L is as low as 3.85 eV, while that for F6 is 10.83 eV (Fig. 4c). As shown in Fig. 4d and Supplementary Fig. 12, the energy evolution of F<sub>6-0</sub> during F atoms departing in F6L is a thermodynamically driven process, totally different from that in F6 with a thermodynamically hindered process.

The electrochemical in-situ FTIR spectroscopy validated the high decomposition tendency of F<sub>6-0</sub> in F6L. The FTIR spectra in attenuated total reflection (ATR) mode were acquired from the simulating Li||Cu half-cells with Blank, F6, and F6L (Supplementary Figs. 15 and 16). Since the main reduction process of Blank occurs at a voltage below 1.0 V (Supplementary Fig. 17), the current response above 1.0 V can boil down to the decomposition of F6L and F6. A strong reduction peak gradually appeared in the F6L cell after the potential reached 2.5 V (*vs.* Li/Li<sup>+</sup>), indicating the fast decomposition of the F6L. By contrast, the decomposition for F6 is difficult, as the reduction peak shown in F6 was located at −1.8 V and exhibited a slightly current response. Moreover, in contrast to F6 and Blank (Fig. 4e and Supplementary Fig. 17), a noticeable infrared C=C signal was detected during the F6L reduction (Fig. 4f). This result corroborates with those from the DFT prediction that the cleavage of C<sup>2</sup>–F and C<sup>3</sup>–F bonds promoted the formation of C<sup>2</sup>=C<sup>3</sup> bonds. Driven by the electrostatic effect of NO<sub>3</sub><sup>−</sup>, the remaining C–F bonds of F<sub>6-0</sub> could be continuously reduced until all six F atoms are lost, giving rise to LiF and possibly Li alkyl carbonates as the final products (Supplementary Fig. 18). By integrating the electrochemical reduction curve and calculating the charge balance (Supplementary Fig. 19), it was confirmed that the overall reduction ratio of F<sub>6-0</sub> in F6L was enlarged from its original 3.1% to 91% after deducting the contribution of the LNO.

### Li plating/stripping analysis

The variations of the interface resistance ( $R_f$ ) of Li symmetric cells during resting were recorded by electrochemical impedance spectroscopy (EIS) to determine the thermodynamic stability of the F6L-derived LiF-rich SEI. The Nyquist plots are shown in Supplementary Fig. 20. The data of the  $R_f$  for Li crossing the SEI were summarized through statistical methods. In Fig. 5a, the  $R_{f,av.}$  is the average  $R_f$ ,  $\sigma_{Rf}$  is the standard deviation, and the  $C_{V,Rf}$  is the coefficient of variation. The  $\sigma_{Rf}$  and  $C_{V,Rf}$  reflects the amplitude of  $R_f$  variation during resting. The  $\sigma_{Rf}$  and  $C_{V,Rf}$  for the F6L cell were lower than those for Blank and F6 cell, which demonstrates that the LiF-rich SEI in F6L possessed excellent thermodynamic stability due to the lower solubility of the LiF in RCE compared to other organic components of SEI; thus, the Li metal could be effectively protected by the SEI away from the electrolyte etching<sup>29</sup>. Compared with the SEI formed in Blank and F6, the

F6L-derived SEI that is featured by LiF-rich and uniform structure has fast Li-ion transport, so the  $R_{f,av.}$  observed in the F6L cell was lower. The temperature-dependent  $R_f$  was characterized using EIS measurements at 0–40 °C, and the activating energy ( $E_{a,Rf}$ ) was calculated by fitting the EIS data to the Arrhenius equation (Supplementary Figs. 21 and 22)<sup>30</sup>. The results show that the F6L cell was with the lowest  $E_{a,Rf}$  (38.5 kJ mol<sup>−1</sup>) among the studied cells (Fig. 5b), so the fast Li-ion transport kinetics in F6L-derived SEI led to a low  $R_{f,av.}$

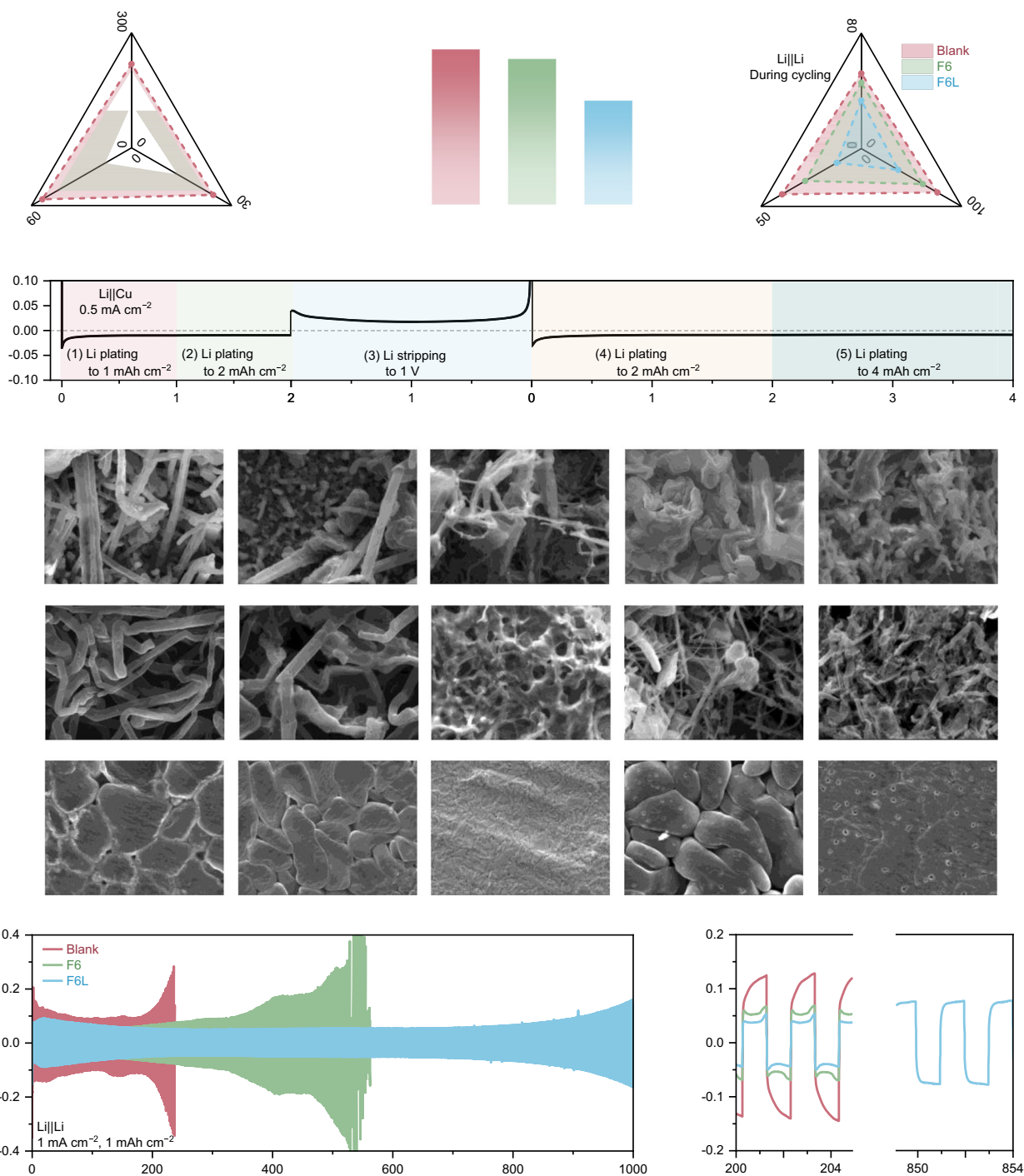
In observation of the  $R_f$  for the Li metal anode during the plating/stripping process, the dynamic structural stability of the SEI can be further estimated. Likewise, three statistical indexes,  $R_{f,av.}$ ,  $\sigma_{Rf}$ , and  $C_{V,Rf}$ , calculated from the three sets of  $R_f$  from the Blank, F6, and F6L cell (Supplementary Fig. 23), were used for the comparison. EIS spectra were measured once every Li plating (0.25 mAh cm<sup>−2</sup>) or stripping (0.25 mAh cm<sup>−2</sup>) occurred. It is evident that the above three indexes for the F6L cell were all lower than those for the other two cells (Fig. 5c), which reveals that the SEI in F6L has not only high structural stability to accommodate the volume fluctuation of the Li plating/stripping but also could restrict the harmful dendrite growth. As was seen in the Li plating/stripping morphologies under various Li deposition conditions (Fig. 5d), the serious dendrite growth was detectable after 1 mAh cm<sup>−2</sup> Li plating on the anodes working in Blank, F6, and RCE + LNO (Fig. 5e, f and Supplementary Fig. 24) due to the local current density derived by the sluggish Li-ion transport and uneven SEI. When Li was cycled in Blank and F6, the dendrite-induced dead Li exacerbated the disorder of Li nucleation and further stimulated the dendrite growth during the subsequent cycles (Supplementary Fig. 25a, b).

The Li cycling morphology in F6L is similar to what is observed in previous literature focusing on the LHCE or HCE<sup>31,32</sup>. The relatively smooth Li deposits with classic island-like morphology were attained in F6L after 1 mAh cm<sup>−2</sup> Li plating (Fig. 5g). More importantly, this dendrite-free morphology could be maintained when the Li capacity reached 2 mAh cm<sup>−2</sup>. It is attributed to the fast Li-ion transport and high Young's modulus of LiF-rich SEI (Supplementary Figs. 26 and 27), significantly dispersing the local current density and promoting uniform Li nucleation/deposition to suppress the dendrite growth. After the total Li stripping, the scanning electron microscope (SEM) image shows a clear and bare Cu substrate, manifesting the highly reversible Li cycling in F6L (Fig. 5g). As a result of the LiF-rich SEI, the Li plating still exhibited large-sized, island-like, and dendrite-free morphology in F6L at the second cycle. Only a flat and dense Li deposition layer was detected even at 4 mAh cm<sup>−2</sup> Li plating. Owing to the synergistic interactions between the F<sub>6-0</sub> and LNO, more F<sub>6-0</sub> molecules were decomposed to contribute to the formation of a LiF-rich SEI, and the Li<sub>3</sub>N from the LNO could also positively work in the SEI tackling the dendrite issues<sup>33</sup>. The cycling performance of the Li symmetric cells exhibited stable 1000-h operations with low voltage hysteresis (Fig. 5h, i), solidly verifying the enhancement aroused by the F6L. By contrast, the lifespan of the F6 and Blank cells was merely 400 and 200 h, respectively.

### Electrochemical performance

The voltage window of the electrolytes was explored by the linear sweep voltammetry (LSV) tests in Fig. 6a. The cut-off voltage for the charging process could reach 5.19 V (*vs.* Li/Li<sup>+</sup>) in F6L since the oxidation process of the F6L at 3.75 V resulted in a stable CEI preferentially formed on the cathode to physically reduce cathode-electrolyte contacts (Supplementary Figs. 28, 29 and Supplementary Table 3). The rate performance of the NCM811||Li full-cell at 4.5 V in various electrolytes, including an LHCE (1.6 M lithium bis(fluorosulfonyl)imide (LiFSI) in 1,2-dimethoxyethane (DME): 1,1,2,2-tetrafluoroethyl 2,2,3,3-tetrafluoropropyl ether (TTE) (1: 1.2: 3 by molar ratio))<sup>31</sup>, are shown in Fig. 6b and Supplementary Fig. 30. Among them, due to the fast Li-ion transport of the LiF-rich SEI, the F6L full-cell with low polarization





delivered the highest state of charge (SOC) over the tests (Fig. 6c), especially after 2 C. The F6, RCE + LNO, and Blank cells exhibited the same attenuation trend in capacity after 0.5 C. Although a LiF-rich SEI was obtained, the lower ionic conductivity of LHCE led to a sharp capacity decay of the cell at 5 C (Supplementary Fig. 31 and

Supplementary Table 4). When the rate back up to 0.5 C, the F6L cell retained a reversible capacity of  $191 \text{ mAh g}^{-1}$ , indicating the high interface stability of the Li metal anode in F6L (Supplementary Fig. 32).

The cycling stability of the full-cells was compared in Fig. 6d. At 0.5 C, the NCM811||Li full-cells (N/P = 2.4) using F6L cycled stably up to

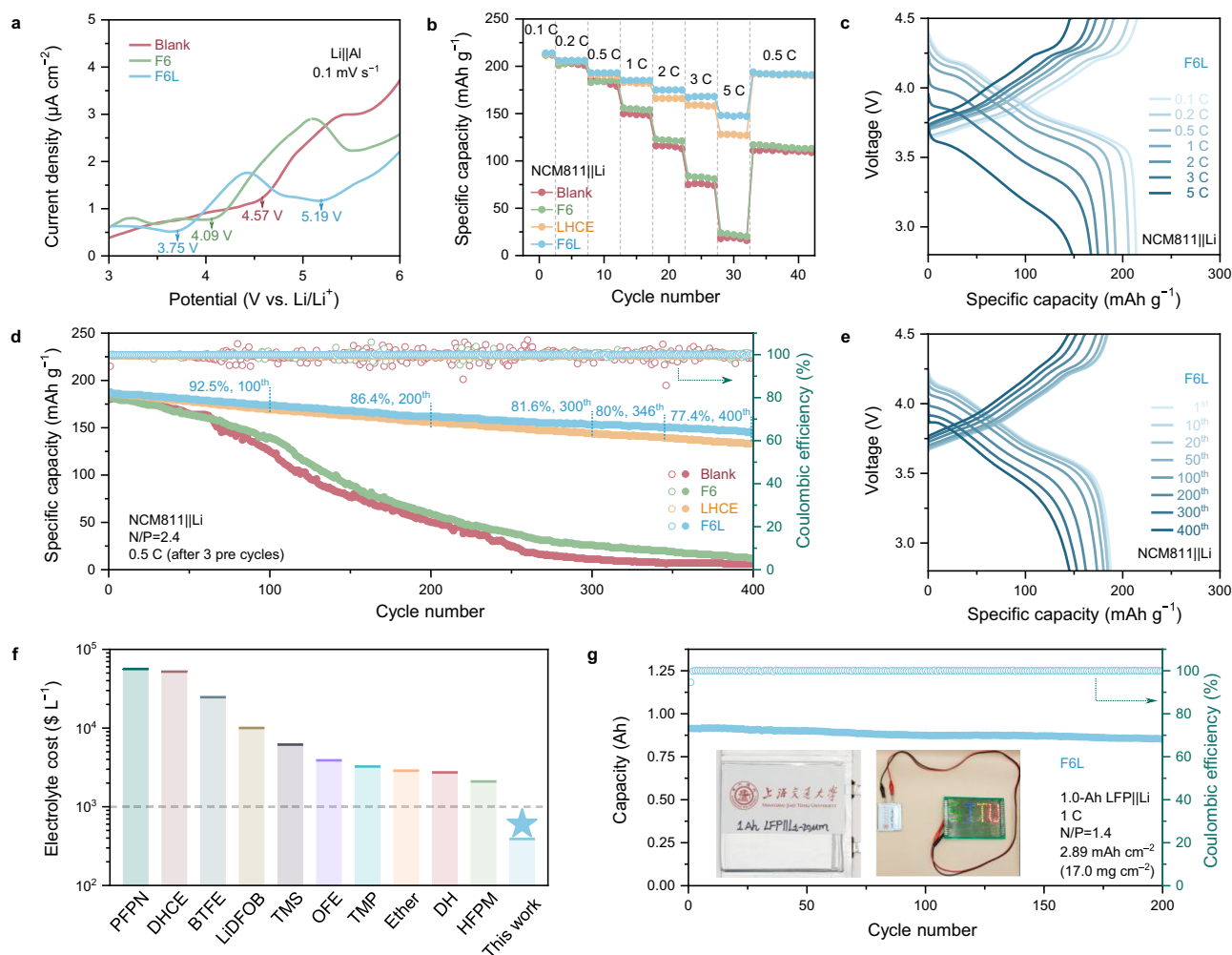


**Fig. 6 | Full-cell performance.** **a** LSV profiles of Li||Al half-cells with Blank, F6, and F6L at a scan rate of 0.1 mV s<sup>-1</sup> from 3 V to 6 V. **b** The rate performance of NCM811||Li full-cells with different electrolytes under the voltage window of 2.8–4.5 V. **c** Voltage profiles of the NCM811||Li full-cell with F6L at various rates. **d** The long-term cycling performance of NCM811||Li full-cells with different electrolytes at 0.5 C. **e** Voltage profiles of the NCM811||Li full-cell with F6L at different cycles. **f** The

comparison of LHCE and HCE strategies with the F6L strategy in cost (PFPN<sup>34</sup>, DHCE<sup>35</sup>, BTFE<sup>36</sup>, LiDFOB<sup>37</sup>, TMS<sup>38</sup>, OFE<sup>39</sup>, TMP<sup>40</sup>, Ether<sup>41</sup>, DH<sup>42</sup>, and HFPM<sup>43</sup>). **g** The cycling performance of the homemade 1.0-Ah LFP||Li pouch cell at 1 C. Insets are digital photos of the pouch cell and the working LED lights. Source data are provided as a Source Data file.

over 400 cycles, exhibiting a 188 mAh g<sup>-1</sup> reversible capacity, lower polarization, and 77.4% retention over cycles (Fig. 6e). In comparison to the related LMB work focusing on the electrolyte additive (Supplementary Table 5), the F6L shows strong competitiveness in terms of elevating the rate performance and service life for LMBs. Pairing with a high areal capacity cathode (3.12 mAh cm<sup>-2</sup>), the F6L cell still showcased an improved cycling performance with a 72.9% capacity retention after 400 cycles (Supplementary Fig. 33). Not surprisingly, the full-cells with F6, RCE + LNO, and Blank experienced a sudden capacity drop over cycles, corresponding to serious anode degradation (Supplementary Figs. 34 and 35). On the other hand, the electrochemical performance of NCM811||Li full-cells in RCE with FEC + LNO, fluoro-benzenes + LNO, fluoroethers + LNO, and other fluoroanhydrides + LNO did not gain satisfying improvement (Supplementary Figs. 36–39), which is largely attributed to their higher C–F bond energy and limited kinetic reductive decomposition (Supplementary Figs. 40–42 and Supplementary Table 6). In addition, the electrochemical performance of the high-voltage LiNi<sub>0.5</sub>Mn<sub>1.5</sub>O<sub>4</sub> (LNMO)||Li full-cell with F6L within the voltage window of 3.5–4.95 V was evaluated, showcasing the high-voltage stability of F6L in the working LMBs (Supplementary Figs. 43 and 44).

The LHCE evidently improves the full-cell cyclability, but its cost is far more than F6L. As shown in Fig. 6f and Supplementary Table 7, the costs of raw materials for the reported LHCE<sup>34–43</sup> are generally more than 1000 \$ L<sup>-1</sup>, while for F6L are as low as 389.8 \$ L<sup>-1</sup>. If considering the 4 vol. % of F6L addition in RCE (the cost of RCE is around 52.6 \$ L<sup>-1</sup>) and the 3 g Ah<sup>-1</sup> of electrolyte addition in each cell, the cost of the F6L strategy is approximately 1.2 \$ Ah<sup>-1</sup>, which is 20 times lower than the cost of LHCE (24.3 \$ Ah<sup>-1</sup>). Therefore, the commercial value of F6L or other F-additives deserves more attention in academics and industry circles.

Furthermore, a homemade 1.0-Ah LFP||Li pouch cell was used to gauge the viability of F6L for practical applications. After a regular activation process at 0.33 C (1 C = 1 Ah), a 93.3% retention was obtained by the F6L pouch cell after 200 cycles at 1 C (Fig. 6g and Supplementary Fig. 45), outperforming the RCE cell. If the cathode loading is increased to 3.5 mAh cm<sup>-2</sup>, the F6L pouch cell could still maintain a high level of capacity retention (92.6%) throughout the cycles (Supplementary Fig. 46). From the above results, a conclusion could be drawn that stabilizing Li anodes by F-additives with a high F/C molar ratio and low decomposition barrier would be another technical line for developing practical LMBs.

## Discussion

In this contribution, a high-quality LiF-rich SEI was formed on the Li metal anode by a low-cost  $F_{6-0}$ /LNO additive to regulate the Li nucleation/deposition in a uniform and dendrite-free manner in RCE. The results demonstrate that the inductive effect on the C–F bond brought by the C=O group can be reduced by  $NO_3^-$ , resulting in the C–F bond cleavage in F6L having lower input energy than in  $F_{6-0}$  alone. This synergistic effect is conducive to improving the overall reduction ratio of  $F_{6-0}$  in F6L up to 91% from its original 3.1%. As a result, a 4 vol. % F6L addition effectively imparted the Li metal anode a LiF-rich SEI with uniform  $Li_3N$  doping in RCE. The Li symmetric cell using F6L achieves a lifespan of more than 1000 h at  $1\text{ mA cm}^{-2}/1\text{ mAh cm}^{-2}$  with a low voltage hysteresis. As expected, the improvement to both NCM811||Li and LNMO||Li full-cells in terms of capacity retention under both high rates and long-term cycles is significantly better by F6L in comparison to the counterparts. More importantly, the F6L strategy also holds the advantage in costs. Our conception of F-additives with a high F/C molar ratio, low decomposition barrier, and reasonable cost offers a route to sustainable and high-performance LMBs, which can also be adapted for other advanced metal-ion batteries.

## Methods

### Materials and chemicals

Hexafluoroglutaric anhydride ( $F_{6-0}$ , **8**), heptafluorobutyric anhydride ( $F_{7-1}$ , **7**), perfluoropropionic anhydride ( $F_{5-1}$ , **9**), tetrafluorosuccinic anhydride ( $F_{4-0}$ , **10**), difluoroacetic anhydride ( $F_{2-1}$ , **11**), fluoroethylene carbonate (FEC, **1**), 1,2-difluorobenzene (F2B, **2**), 2,3-difluorotoluene (F2T, **3**), benzotrifluoride (F3T, **4**), 1,1,2,2-tetrafluoroethyl 2,2,3,3-tetrafluoropropyl ether (TTE, also commonly abbreviated as HFE, **5**), 1,1,2,2-tetrafluoroethyl 2,2,2-trifluoroethyl ether (TFETFE, **6**), and 1,2-dimethoxyethane (DME) were purchased from Adamas-beta. The RCE of 1.0 M  $LiPF_6$  in EC/DMC (1: 1, v/v) used as Blank was purchased from DoDoChem Co., Limited. Lithium bis(fluorosulfonyl)azanide ( $LiFSI$ ), lithium hexafluorophosphate ( $LiPF_6$ ), and Lithium nitrate (LNO) were purchased from DoDoChem Co., Limited. Lithium salts and solvents applied in this experiment were all in battery-grade. Li metal foils were purchased from China Energy Lithium Co., Limited, wherein Li-20  $\mu\text{m}$  was used as the anode, and Li-450  $\mu\text{m}$  ( $\Phi$  15.6 mm) was used as an excessive Li source. The  $LiNi_{0.8}Co_{0.1}Mn_{0.1}O_2$  (NCM811) cathode with different loading (8.05 and 14.87  $\text{mg cm}^{-2}$ ) was purchased from Canrd New Energy Technology Co., Limited. The  $LiNi_{0.5}Mn_{1.5}O_4$  (LNMO) (9.03  $\text{mg cm}^{-2}$ ) cathode was purchased by Beijing Li-Volt Energy Technology Co., Limited. The 1.0-Ah and 1.21-Ah  $LiFePO_4$ ||Li-20  $\mu\text{m}$  (LFP||Li) pouch cells were self-made (Supplementary Table 8).

### Cell preparation

Electrochemical tests were carried out using CR2032-type coin cells and Celgard 2325 separators. All electrolytes and cells were prepared and assembled in an Ar-filled glove box ( $O_2 < 0.01\text{ ppm}$ ,  $H_2O < 0.01\text{ ppm}$ ). All electrodes were cut into a diameter of 12 mm. 40  $\mu\text{L}$  electrolyte was added in each coin cell for testing. 3 g  $Ah^{-1}$  electrolyte was added in each pouch cell for testing. A comprehensive compilation of the full-cells' parameters, encompassing electrode materials, separator properties, and procedural details, was presented in Supplementary Table 9. Unless otherwise specified, all tests were conducted at room temperature.

### Electrochemical measurements

Land CT2001 and Neware CT-4008 multichannel battery tester were employed to monitor cell performance. EIS and LSV measurements were performed on a Bio-logic VMP300 electrochemical workstation. EIS measurements were carried out at a voltage amplitude of 10 mV and in a frequency range of 100 kHz–100 mHz.

## Characterizations

The morphology was characterized by SEM (JSM 7401F) and cryo-TEM (Spectra 300). FTIR (Nicolet 6700) spectroscopy in ATR mode with an electrochemical workstation was applied to detect the growth process of SEI. The Ar-ion etching-assisted XPS was collected using a Kratos AXIS UltraDLD X-ray photoelectron spectrometer excited by monochromatic Al (1486.7 eV, 240 W) source. TOF-SIMS (GAIA3) was applied to investigate the spatial stereoscopic distribution of SEI. NMR (Avance III 400 MHz) measurement was used to detect  $^{19}\text{F}$  signals in different electrolytes.

## Ionic models and computational methods

The molecular geometry optimizations of DMC, EC, and  $F_{6-0}$  were performed at the B3LYP/6-311+G(d,p) level of theory<sup>44</sup>, as implemented in the Gaussian 16 package<sup>45</sup>. The decomposition processes of F6 and F6L molecules under electrolyte conditions were considered, primarily involving reactions with surrounding salt molecules. Both F6 and F6L modeling systems were constructed using the GROMACS package with cubic periodic boundary conditions<sup>46</sup> for molecular dynamics (MD) simulations. The atomistic force field parameters for all ions and molecules were described using the AMBER format, as reported in a previous work<sup>47</sup>. The cross-interaction parameters for different atom types were derived using the Lorentz–Berthelot combination rules<sup>48</sup>. The equations governing atomic motion were integrated using the Verlet leapfrog algorithm<sup>49</sup> with a 1.0 fs time step. A cut-off radius of 1.6 nm was set for short-range van der Waals and real-space electrostatic interactions. The particle-mesh Ewald (PME) summation method<sup>50</sup>, with an interpolation order of 5 and a Fourier grid spacing of 0.20 nm, was used to handle long-range electrostatic interactions in reciprocal space.

In MD calculations, both simulation systems were first energetically minimized using a steepest descent algorithm, and thereafter annealed gradually from 600 K to 300 K (room temperature) within 10 ns. Then, the systems were equilibrated at 300 K and 1 atm in an isothermal-isobaric (NPT) ensemble for 20 ns to obtain the optimal system sizes. The temperature was controlled by a Nosé–Hoover thermostat and the pressure by a Parrinello–Rahman barostat, with time coupling constants of 0.4 ps and 0.2 ps, respectively. The optimal sizes and compositions of the modeling systems are listed in Supplementary Table 10. Atomistic simulations were further conducted at 300 K in a canonical ensemble (NVT) for 50 ns, with a time coupling constant of 0.4 ps for the Nosé–Hoover thermostat. The simulation trajectories were recorded every 100 fs for further structural and thermodynamic analysis.

Additional DFT calculations were performed to determine the decomposition processes of the  $F_{6-0}$  molecule with and without LNO. The calculations were performed using the Gaussian 16 package<sup>45</sup> at the same level of theory: B3LYP/6-311+G(d,p)<sup>44</sup> with Grimme's D3 (GD3BJ) dispersion correction. The optimized coordination structures and Bader charges<sup>51</sup> of representative intermediates along the reaction coordinates were determined, and the corresponding energy barriers were extracted.

## Computational method of the reduction ratio of $F_{6-0}$

Electrolyte loading in the separator: The parameters of the separator can be used to determine the electrolyte loading volume, as follows,

$$V = \frac{\pi D^2}{4} h \phi = \frac{3.14 \times (15.6\text{ mm})^2}{4} \times 25\text{ }\mu\text{m} \times 0.39 = 1.86 \times 10^{-9}\text{ m}^3 = 1.86\text{ }\mu\text{L} \quad (1)$$

Where the  $\phi$  is the porosity of the separator. Considering the irreversible consumption of a portion to form SEI, the amount of electrolyte used was doubled, namely 3.72  $\mu\text{L}$ , in order to maintain the normal circuit during the reduction process.

Calculating the charge balance of  $F_{6-0}$ : As an additive in RCE, assuming that  $F_{6-0}$  is completely reduced to form LiF, the corresponding charge amount is as follows,

$$Q_{F_{6-0}} = \frac{3.72 \mu\text{L} \times 4 \text{ vol. \% } \rho_{F_{6-0}} N_A}{M_{F_{6-0}}} \times 6e$$

$$= \frac{3.72 \mu\text{L} \times 4 \text{ vol. \% } \times 1.65 \text{ g mL}^{-1} \times 6.02 \times 10^{23} \text{ mol}^{-1}}{222.04 \text{ g mol}^{-1}} \times 6e = 4.0 \times 10^{18} e \quad (2)$$

Where the  $\rho$  is the density,  $N_A$  is the Avogadro constant,  $M$  is the relative atomic mass, and  $e$  is the elementary charge ( $1e = 1.6 \times 10^{-19} \text{ C}$ ).

Integral and unit conversion: The electrochemical reduction curves of Supplementary Fig. 19 were integrated, respectively, as follows,

$$\int_3^0 I_{\text{Blank}}(U) dU = 5.20 \mu\text{A cm}^{-2} \text{ V} \quad (3)$$

$$\int_3^0 I_{F_6}(U) dU = 6.25 \mu\text{A cm}^{-2} \text{ V} \quad (4)$$

$$\int_3^0 I_{F_{6L}}(U) dU = 46.02 \mu\text{A cm}^{-2} \text{ V} \quad (5)$$

Where the  $I$  is the current (density),  $U$  is the voltage (potential). The voltage sweep rate was a constant of  $0.1 \text{ mV s}^{-1}$  and the cross-sectional area with a diameter of  $15.6 \text{ mm}$  is  $1.91 \text{ cm}^2$ . Therefore, the corresponding amount of charge can be obtained, as follows,

$$q_{\text{Blank}} = \frac{5.20 \mu\text{A cm}^{-2} \text{ V} \times 1.91 \text{ cm}^2}{0.1 \text{ mV s}^{-1}} = 9.93 \times 10^{-2} \text{ As} = 9.93 \times 10^{-2} \text{ C} = 6.20 \times 10^{17} e \quad (6)$$

$$q_{F_6} = \frac{6.25 \mu\text{A cm}^{-2} \text{ V} \times 1.91 \text{ cm}^2}{0.1 \text{ mV s}^{-1}} = 1.19 \times 10^{-1} \text{ As} = 1.19 \times 10^{-1} \text{ C} = 7.45 \times 10^{17} e \quad (7)$$

$$q_{F_{6L}} = \frac{46.02 \mu\text{A cm}^{-2} \text{ V} \times 1.91 \text{ cm}^2}{0.1 \text{ mV s}^{-1}} = 8.79 \times 10^{-1} \text{ As} = 8.78 \times 10^{-1} \text{ C} = 5.49 \times 10^{18} e \quad (8)$$

Where the  $q$  is the quantity of electric charge.

Calculating the reduction ratio  $F_{6-0}$  in F6: Subtracting Eq. (6) from Eq. (7) yields the amount of charge exchanged by  $F_{6-0}$  during the reduction process. Therefore, the reduction ratio of  $F_{6-0}$  in F6 is

$$\frac{q_{F_6} - q_{\text{Blank}}}{Q_{F_{6-0}}} \times 100\% = \frac{7.45 \times 10^{17} e - 6.20 \times 10^{17} e}{4.0 \times 10^{18} e} \times 100\% = 3.1\% \quad (9)$$

Calculating the reduction ratio  $F_{6-0}$  in F6L: Subtracting Eq. (6) from Eq. (8) yields the amount of charge exchanged by F6L during the reduction process. Considering that LNO can also be reduced to form  $\text{Li}_3\text{N}$  with charge exchanged and the molar ratio of  $F_{6-0}$  to LNO in F6L is 3.96: 1, the reduction ratio  $F_{6-0}$  in F6L after deducting the contribution of the LNO is

$$\frac{(q_{F_{6L}} - q_{\text{Blank}}) \times \frac{3.96 \times 6e}{3.96 \times 6e + 1 \times 8e}}{Q_{F_{6-0}}} \times 100\%$$

$$= \frac{(5.49 \times 10^{18} e - 6.20 \times 10^{17} e) \times \frac{3.96 \times 6e}{3.96 \times 6e + 1 \times 8e}}{4.0 \times 10^{18} e} \times 100\% = 91\% \quad (10)$$

Analysis of the rationality of the computational method for the reduction ratio of  $F_{6-0}$ : Considering the reduction peak positions of different components obtained from LSV testing, the calculated  $F_{6-0}$  reduction ratio (91%) in F6L, based on the molar ratio of  $F_{6-0}$  to LNO, is a conservative approach, ensuring that the actual reduction ratio of  $F_{6-0}$  in F6L is at least 91% (Supplementary Fig. 47). Furthermore, through LSV tests with different concentrations of LNO in RCE, the reduction ratios at these concentrations were obtained (Supplementary Fig. 48). Thus, the differential method mentioned above allows for the quantitative calculation of the additive's reduction ratio, proving it to be feasible.

## Reporting summary

Further information on research design is available in the Nature Portfolio Reporting Summary linked to this article.

## Data availability

The datasets generated during and/or analyzed during the current study are available from the corresponding author on reasonable request. Source data are provided with this paper. Figshare <https://doi.org/10.6084/m9.figshare.27021079> Source data are provided with this paper.

## References

- Zhang, S. & Chen, W. Assessing the energy transition in China towards carbon neutrality with a probabilistic framework. *Nat. Commun.* **13**, 87 (2022).
- Wang, J. et al. Improving cyclability of Li metal batteries at elevated temperatures and its origin revealed by cryo-electron microscopy. *Nat. Energy* **4**, 664–670 (2019).
- Chen, X., Zhan, B., Yan, C. & Zhang, Q. Review on Li deposition in working batteries: from nucleation to early growth. *Adv. Mater.* **33**, 2004128 (2021).
- Liu, Y. et al. Self-assembled monolayers direct a LiF-rich interphase toward long-life lithium metal batteries. *Science* **375**, 739–745 (2022).
- Zhuang, H. et al. LiF-rich alloy-doped SEI enabling ultra-stable and high-rate Li metal anode. *Angew. Chem. Int. Ed.* **63**, e202407315 (2024).
- Yang, T. et al. Stable LiF-rich electrode–electrolyte interface toward high-voltage and high-energy-density lithium metal solid batteries. *Small* **19**, 2300494 (2023).
- Huang, K. et al. In-situ formation of LiF-rich solid-electrolyte interphases on 3D lithiophilic skeleton for stable lithium metal anode. *Energy Storage Mater.* **55**, 301–311 (2023).
- Tan, J., Matz, J., Dong, P. & Ye, M. A growing appreciation for the role of LiF in the solid electrolyte interphase. *Adv. Energy Mater.* **11**, 2100046 (2021).
- Wan, H., Xu, J. & Wang, C. Designing electrolytes and interphases for high-energy lithium batteries. *Nat. Rev. Chem.* **8**, 30–44 (2024).
- Yu, Z. et al. Molecular design for electrolyte solvents enabling energy-dense and long-cycling lithium metal batteries. *Nat. Energy* **5**, 526–533 (2020).
- Xue, W. et al. FSI-inspired solvent and “full fluorosulfonyl” electrolyte for 4 V class lithium-metal batteries. *Energy Environ. Sci.* **13**, 212–220 (2020).
- Yu, Z. et al. Rational solvent molecule tuning for high-performance lithium metal battery electrolytes. *Nat. Energy* **7**, 94–106 (2022).
- Cao, X., Jia, H., Xu, W. & Zhang, J. Review—localized high-concentration electrolytes for lithium batteries. *J. Electrochem. Soc.* **168**, 010522 (2021).
- Jia, H. et al. High-performance silicon anodes enabled by non-flammable localized high-concentration electrolytes. *Adv. Energy Mater.* **9**, 1900784 (2019).



15. Wang, T. et al. Dual-salts localized high-concentration electrolyte for Li- and Mn-rich high-voltage cathodes in lithium metal batteries. *Small* **20**, 2401364 (2024).
16. Zhang, J. et al. Diluent decomposition-assisted formation of LiF-rich solid-electrolyte interfaces enables high-energy Li-metal batteries. *J. Energy Chem.* **78**, 71–79 (2023).
17. Zheng, J. et al. Electrolyte additive enabled fast charging and stable cycling lithium metal batteries. *Nat. Energy* **2**, 17012 (2017).
18. Zhang, W. et al. Tuning the LUMO energy of an organic interphase to stabilize lithium metal batteries. *ACS Energy Lett.* **4**, 644–650 (2019).
19. Zhou, P. et al. Rationally designed fluorinated amide additive enables the stable operation of lithium metal batteries by regulating the interfacial chemistry. *Nano Lett.* **22**, 5936–5943 (2022).
20. Xu, N. et al. Research progress of fluorine-containing electrolyte additives for lithium ion batteries. *J. Power Sources Adv.* **7**, 100043 (2021).
21. Ding, J. et al. Non-solvating and low-dielectricity cosolvent for anion-derived solid electrolyte interphases in lithium metal batteries. *Angew. Chem. Int. Ed.* **60**, 11442–11447 (2021).
22. Heiskanen, S. K. & Lucht, B. L. Fluorinated acetic anhydrides as electrolyte additives to improve cycling performance of the lithium metal anode. *J. Electrochem. Soc.* **167**, 110506 (2020).
23. Yang, H. et al. Dissolution–precipitation dynamics in ester electrolyte for high-stability lithium metal batteries. *ACS Energy Lett.* **6**, 1413–1421 (2021).
24. Aurbach, D., Youngman, O., Gofer, Y. & Meitav, A. The electrochemical behavior of 1,3-dioxolane—LiClO<sub>4</sub> solutions—I. Uncontaminated solutions. *Electrochim. Acta* **35**, 625–638 (1990).
25. Adams, B. D., Zheng, J., Ren, X., Xu, W. & Zhang, J. Accurate determination of Coulombic efficiency for lithium metal anodes and lithium metal batteries. *Adv. Energy Mater.* **8**, 1702097 (2018).
26. Han, J., Kim, K., Lee, Y. & Choi, N. Scavenging materials to stabilize LiPF<sub>6</sub>-containing carbonate-based electrolytes for Li-ion batteries. *Adv. Mater.* **31**, 1804822 (2019).
27. Spotte-Smith, E. W. C., Petrocelli, T. B., Patel, H. D., Blau, S. M. & Persson, K. A. Elementary decomposition mechanisms of lithium hexafluorophosphate in battery electrolytes and interphases. *ACS Energy Lett.* **8**, 347–355 (2023).
28. Heo, J. et al. Electro-inductive effect: electrodes as functional groups with tunable electronic properties. *Science* **370**, 214–219 (2020).
29. Yan, C. et al. Toward critical electrode/electrolyte interfaces in rechargeable batteries. *Adv. Funct. Mater.* **30**, 1909887 (2020).
30. Mertens, A. et al. Quantitative analysis of time-domain supported electrochemical impedance spectroscopy data of Li-ion batteries: reliable activation energy determination at low frequencies. *J. Electrochem. Soc.* **163**, H521 (2016).
31. Ren, X. et al. Enabling high-voltage lithium-metal batteries under practical conditions. *Joule* **3**, 1662–1676 (2019).
32. Ren, X. et al. Localized high-concentration sulfone electrolytes for high-efficiency lithium-metal batteries. *Chem* **4**, 1877–1892 (2018).
33. Park, K. & Goodenough, J. B. Dendrite-suppressed lithium plating from a liquid electrolyte via wetting of Li<sub>3</sub>N. *Adv. Energy Mater.* **7**, 1700732 (2017).
34. Zhang, C. et al. Nonflammable, localized high-concentration electrolyte towards a high-safety lithium metal battery. *Energy Storage Mater.* **52**, 355–364 (2022).
35. Liu, Q. et al. An inorganic-dominate molecular diluent enables safe localized high concentration electrolyte for high-voltage lithium-metal batteries. *Adv. Funct. Mater.* **33**, 2209725 (2023).
36. Yu, L. et al. A localized high-concentration electrolyte with optimized solvents and lithium difluoro(oxalate)borate additive for stable lithium metal batteries. *ACS Energy Lett.* **3**, 2059–2067 (2018).
37. Wang, W. et al. Stable cycling of high-voltage lithium-metal batteries enabled by high-concentration FEC-based electrolyte. *ACS Appl. Mater. Interfaces* **12**, 22901–22909 (2020).
38. Lin, S., Hua, H., Lai, P. & Zhao, J. A multifunctional dual-salt localized high-concentration electrolyte for fast dynamic high-voltage lithium battery in wide temperature range. *Adv. Energy Mater.* **11**, 2101775 (2021).
39. Huangzhang, E. et al. A localized high-concentration electrolyte with lithium bis(fluorosulfonyl) imide (LiFSI) salt and F-containing cosolvents to enhance the performance of Li||LiNi<sub>0.8</sub>Co<sub>0.1</sub>Mn<sub>0.1</sub>O<sub>2</sub> lithium metal batteries. *Chem. Eng. J.* **439**, 135534 (2022).
40. Jia, M. et al. Advanced nonflammable localized high-concentration electrolyte for high energy density lithium battery. *Energy Environ. Mater.* **5**, 1294–1302 (2022).
41. Li, T., Li, Y., Sun, Y., Qian, Z. & Wang, R. New insights on the good compatibility of ether-based localized high-concentration electrolyte with lithium metal. *ACS Mater. Lett.* **3**, 838–844 (2021).
42. Lin, S., Hua, H., Li, Z. & Zhao, J. Functional localized high-concentration ether-based electrolyte for stabilizing high-voltage lithium-metal battery. *ACS Appl. Mater. Interfaces* **12**, 33710–33718 (2020).
43. Dai, W. et al. Localized concentrated high-concentration electrolyte enhanced stability and safety for high voltage Li-ion batteries. *Electrochim. Acta* **320**, 134633 (2019).
44. Becke, A. D. Density-functional thermochemistry. III. The role of exact exchange. *J. Chem. Phys.* **98**, 5648–5652 (1990).
45. Frisch, M. J. et al. *Gaussian 16, Revision C.01* (Gaussian, Inc., Wallingford, CT, 2016).
46. Abraham, M. J. et al. GROMACS: High performance molecular simulations through multi-level parallelism from laptops to supercomputers. *SoftwareX* **1–2**, 19–25 (2015).
47. Wang, Y., Shah, F. U., Glavatskih, S., Antzutkin, O. N. & Laaksonen, A. Atomistic insight into orthoborate-based ionic liquids: force field development and evaluation. *J. Phys. Chem. B* **118**, 8711–8723 (2014).
48. Forsman, J. & Woodward, C. E. Limitations of the Derjaguin approximation and the Lorentz–Berthelot mixing rule. *Langmuir* **26**, 4555–4558 (2010).
49. Bufolo, G. N. & Sobral, Y. D. Analysis of the leapfrog-Verlet method applied to the Kuwabara-Kono force model in discrete element method simulations of granular materials. *Adv. Comput. Math.* **50**, 82 (2024).
50. Petersen, H. G. Accuracy and efficiency of the particle mesh Ewald method. *J. Chem. Phys.* **103**, 3668–3679 (1995).
51. Yu, M. & Trinkle, D. R. Accurate and efficient algorithm for Bader charge integration. *J. Chem. Phys.* **134**, 064111 (2011).

## Acknowledgements

This work was supported by the National Natural Science Foundation of China (NSFC) under Grant No. 22379093 (Z.L.), 52102282 (Z.L.), the Fundamental Research Funds for the Central Universities No. 22X010201631 (Z.L.), 23X010301599 (Z.L.).

## Author contributions

J.L., W.H., M.F., and X.Y. conducted the experiments, analyzed the data, and wrote the manuscript. W.H. developed the ionic models, performed the DFT calculations, and revised the manuscript. M.F. performed the electrochemical tests and analyzed the data. X.C., M.F., and Y.D. analyzed the data and revised the manuscript. X.C., Y.C., and Z.W. provided discussions with electrochemical tests. X.C. wrote the cover letter. X.Y. and Z.L. conceived the idea, supervised the work, and revised the manuscript. All authors contributed to the scientific discussion of the manuscript.

## Competing interests

The authors declare no competing interests.



## Additional information

**Supplementary information** The online version contains supplementary material available at <https://doi.org/10.1038/s41467-024-53807-z>.

**Correspondence** and requests for materials should be addressed to Xinyang Yue or Zheng Liang.

**Peer review information** *Nature Communications* thanks the anonymous reviewer(s) for their contribution to the peer review of this work. A peer review file is available.

**Reprints and permissions information** is available at <http://www.nature.com/reprints>

**Publisher's note** Springer Nature remains neutral with regard to jurisdictional claims in published maps and institutional affiliations.

**Open Access** This article is licensed under a Creative Commons Attribution-NonCommercial-NoDerivatives 4.0 International License, which permits any non-commercial use, sharing, distribution and reproduction in any medium or format, as long as you give appropriate credit to the original author(s) and the source, provide a link to the Creative Commons licence, and indicate if you modified the licensed material. You do not have permission under this licence to share adapted material derived from this article or parts of it. The images or other third party material in this article are included in the article's Creative Commons licence, unless indicated otherwise in a credit line to the material. If material is not included in the article's Creative Commons licence and your intended use is not permitted by statutory regulation or exceeds the permitted use, you will need to obtain permission directly from the copyright holder. To view a copy of this licence, visit <http://creativecommons.org/licenses/by-nc-nd/4.0/>.

© The Author(s) 2024